Faraday Discussions

Cite this: Faraday Discuss., 2016, 193, 51



PAPER

View Article Online View Journal | View Issue

Electrochemistry at single molecule occupancy in nanopore-confined recessed ring-disk electrode arrays

Kaiyu Fu,^a Donghoon Han,^b Chaoxiong Ma^a and Paul W. Bohn*ab

Received 30th March 2016, Accepted 4th April 2016

DOI: 10.1039/c6fd00062b

Electrochemical reactions at nanoscale structures possess unique characteristics, e.g. fast mass transport, high signal-to-noise ratio at low concentration, and insignificant ohmic losses even at low electrolyte concentrations. These properties motivate the fabrication of high density, laterally ordered arrays of nanopores, embedding vertically stacked metal-insulator-metal electrode structures and exhibiting precisely controlled pore size and interpore spacing for use in redox cycling. These nanoscale recessed ring-disk electrode (RRDE) arrays exhibit current amplification factors, AF_{RC}, as large as 55-fold with $Ru(NH_3)_6^{2/3+}$, indicative of capture efficiencies at the top and bottom electrodes, $\Phi_{\rm thr}$ exceeding 99%. Finite element simulations performed to investigate the concentration distribution of redox species and to assess operating characteristics are in excellent agreement with experiment. AF_{RC} increases as the pore diameter, at constant pore spacing, increases in the range 200-500 nm and as the pore spacing, at constant pore diameter, decreases in the range 1000-460 nm. Optimized nanoscale RRDE arrays exhibit a linear current response with concentration ranging from $0.1 \,\mu\text{M}$ to 10 mM and a small capacitive current with scan rate up to $100~{
m V}~{
m s}^{-1}$. At the lowest concentrations, the average pore occupancy is $\langle n \rangle \sim 0.13$ molecule establishing productive electrochemical signals at occupancies at and below the single molecule level in these nanoscale RRDE arrays.

Introduction

The rapid development of nanofabrication techniques has enabled electrochemical experiments with electrodes in the nanoscale regime. 1,2 Typically this has been realized by fabricating ultrasmall electrodes with critical dimensions below 100 nm that exhibit unique electrochemical properties, e.g. sigmoidal voltammetric response, negligible ohmic (iR) potential losses, and small intrinsic

^aDepartment of Chemistry and Biochemistry, University of Notre Dame, Notre Dame, IN 46556, USA. E-mail: pbohn@nd.edu

^bDepartment of Chemical and Biomolecular Engineering, University of Notre Dame, Notre Dame, IN 46556,

charging currents.^{3,4} Nanoelectrodes have also been employed to advantage in investigations of mass transport and electron transfer with enhanced temporal and spatial resolution.^{5,6} Many reports focus on the fabrication of single nanoelectrodes with characteristic sizes ranging from a few nanometers to >100 nm, ⁷⁻⁹ however, when compared to macroscopic electrodes, or even microelectrodes, the current is limited, and achieving device-to-device reproducibility is challenging. Nanoelectrode ensembles (NEEs)10,11 and nanoelectrode arrays (NEAs)12-14 have been fabricated to increase the measurable current while maintaining the large bandwidth benefits of nanoelectrodes. 15 Recently, we have explored massively parallel arrays of NEAs fabricated with dual electrodes embedded in nanopores and operated in redox cycling (RC) mode, either with or without supporting electrolyte.16-21

In RC mode, reversible electro-active species undergo successive oxidation and reduction reactions by cycling between two closely-spaced, independentlyaddressable electrodes, i.e. electroactive molecules that are oxidized at one electrode then move to the other electrode and are reduced, then they can move back to the anode and repeat the cycle.22 Pioneering work on RC was accomplished with rotating ring-disc electrodes^{23,24} and interdigitated array electrodes,²⁵⁻²⁷ which used forced convection and the small size (5-50 μm, typically) of the interelectrode gap, respectively, to amplify current. Bard and coworkers²⁸⁻³⁰ extended the electrode spacing concept in an elegant way to directly detect current resulting from redox cycling of single molecules in a small volume trapped between a surface and a scanning electrochemical microscopy tip. Improvements in nanofabrication technology have made it possible to fabricate more precise RC systems, e.g. nanofluidic channels with closely parallel electrodes, 31,32 nanogap electrodes enclosing attoliter volumes, 33 and nanopore-based arrays with recessed ring-disk electrodes20 have all been designed for ultrasensitive electrochemical measurements. Nanopore-based electrodes constitute a special class of nanoscale RC systems, because redox species are confined and can become electrostatically trapped such that they react with both electrodes multiple times before diffusing out of the nanopore.

In order to produce nanopore-based RC systems with control over geometric parameters, such as pore size, density and interpore distance, advanced lithographic techniques, e.g., electron-beam lithography (EBL) and focused ion beam (FIB) milling, have been employed. For example, Wolfrum and co-workers³⁴ reported an approach to high density nanopore electrode arrays by combining EBL and reaction ion etching (RIE). Recently, our group took advantage of FIB milling to fabricate high density ($\sim 2 \times 10^9 \text{ cm}^{-2}$) dual-ring nanopore electrode arrays which exhibit enhanced electrochemical performance.21 However, these techniques are restricted by the need for serial-write lithography processes, employ expensive facilities, are time-consuming, and produce low throughput, so they are not well-suited to fabricating high density patterns at large scale.

Nanosphere lithography (NSL), also known as colloidal lithography, is based on the natural self-assembly of colloidal particle templates on substrates and was introduced by Fischer and Zingsheim in 1981.35 Since then, by using smaller size nanospheres36,37 and well-designed coating methods,38,39 nanostructured arrays with elements smaller than 100 nm have been achieved with long-range order over large distances. We have used this procedure to develop sub-micrometer arrays with dual electrodes, demonstrating excellent sensitivity and selectivity in voltammetric measurements. 17,19

Here, we extend the geometry of NSL-templated recessed ring-disk electrode (RRDE) arrays to small spacings (<500 nm) and large pore densities (up to 10⁹ pores per cm²) and explore the dependence of voltammetric response on the geometry of the array, including pore size and inter-pore spacing, in order to produce structures capable of redox cycling under single molecule occupancy conditions. By varying the size of the nanospheres in the template and the exposure time to O₂ plasma etching, nanopore electrode arrays with a wide range of pore diameters (800 nm to 100 nm) and pore densities (108 to 109 pores per cm²) have been achieved with good uniformity at large scale. The optimized RRDE arrays demonstrate high collection efficiency in RC mode, producing current amplification as large as 55-fold. At the lowest concentrations examined, this performance is sufficient to achieve electrochemical measurements at single molecule occupancy levels, i.e. signals are obtained from a parallel array of nanopores, each containing $n \le 1$ molecules, with the single molecule cycling between the lower (disk) and upper (ring) electrodes. The dependence of voltammetric behavior on the potential of the generator and collector electrodes, and the size and spacing of the nanopores in RC mode has been investigated experimentally and compared with the results of finite element simulations, showing that both pore diameter and pore density are important factors that govern transport-limited electron transfer and the corresponding current amplification. These structures also exhibit a linear current response over a wide range of analyte concentration and exhibit remarkably small capacitive currents, even at very fast scan rates.

Experimental section

Chemicals and materials

Hexaammineruthenium chloride ([Ru(NH₃)₆]Cl₃), potassium chloride, sulfuric acid (95%), and hydrogen peroxide (30%) were obtained from Sigma-Aldrich and used as received. Deionized (DI) water was generated from a Milli-Q Gradient water purification system (Millipore). Photoresist AZ5214E (AZ Electronic Materials) and polydimethylsiloxane (PDMS) (Dow Corning) were used according to the manufacturers' specifications.

Device fabrication

High density RRDE arrays were fabricated by using photolithography, layer-by-layer deposition, nanosphere lithography (NSL), and multiple reactive ion etching (RIE), similar to previously reported procedures.²⁰ A glass slide was cleaned in piranha solution (3 : 1 sulfuric acid (95%) : hydrogen peroxide (30%) – **caution** – strong oxidizer, use with extreme care) for 1 h, rinsed with DI water, and then dried at 100 °C for 2 h. A negative photoresist (AZ5214E) was used to define the overall pattern of the bottom electrode on glass. A 95 nm thick Au film, with a 5 nm Cr adhesion layer, was deposited using electron-beam evaporation (UNIVEX 450B, Oerlikon). After metal lift-off, a 50 nm thick SiN_x layer was then deposited by plasma-enhanced chemical vapor deposition (PECVD 790, Plasma-Therm). Then the overall top electrode pattern was deposited perpendicular to and

overlapping the bottom electrode using the same photolithography procedure. The area of top and bottom electrode layer overlap was 180 μ m \times 180 μ m. Next, an additional 200 nm thick SiO₂ layer was deposited over the whole surface to passivate the top surface. The substrate was exposed briefly to an O2 plasma (Drytek RF Plasma asher, 1500W) to make the surface hydrophilic and then was immediately stored in DI water. Then a highly ordered polystyrene (PS) nanosphere monolayer was prepared at a liquid-air interface and was transferred to the substrate by immersing it at \sim 45° through the interface. Once the substrate was dried in air, O2 plasma etching (Plasmatherm 790, 100W) was used to reduce the nanosphere size - with longer exposure times producing smaller final nanospheres. Then a metal nanopore mask was produced by depositing a 10 nm thick Cr film on top of the SiO₂ layer and then removing the PS nanospheres by sonication in chloroform or acetone for 5 min. Afterwards, a square pattern (150 μ m \times 150 μm) at the center of the intersection area was defined by photolithography to act as an overall etch mask for subsequent dry etching. Finally, the RRDE arrays were produced by transferring the pattern through the template using multistep reactive ion etching (Plasmatherm 790). During etching, each upper layer acts as the etch mask for the layer below it, e.g., the Cr layer protects the SiO2 layer, the SiO₂ protects the Au layer, etc.

Modeling and calculations

Modeling calculations were performed using finite element simulation software (COMSOL Multiphysics 5.0). The electrochemical system treated here is a simple outer-sphere heterogeneous electron transfer reaction at the electrodes, O + ne⁻ \rightleftharpoons R, where n is the number of electrons transferred. The arrays were simulated in a 2D geometry, consisting of recessed disk electrodes, a 50 nm thick insulating layer, a 100 nm thick ring electrode layer, and a 200 nm thick top insulator layer. The domain above the pores was drawn sufficiently large to avoid interference from boundaries, and the mesh was refined both within the nanopores and in the region just above the pores to avoid misleading results. For the case of high overpotential applied to the electrodes, constant-concentration boundary conditions were applied based on the assumption of complete oxidation or complete reduction on the electrode surfaces. The various devices were characterized at steady-state by assuming that the diffusion coefficients of the reduced and oxidized forms are the same, leading to the result that the sum of oxidized (C_0) and reduced (C_R) forms is constant over the diffusion space and is equal to the sum of the bulk concentrations (C_{bulk}).

Electrochemical measurements

Cyclic voltammetry (CV) experiments were performed with a CH Instruments electrochemical analyzer (Model 842C) using a Pt wire and Ag/AgCl as auxiliary and reference electrodes, respectively. The top and bottom electrodes of the RRDE arrays were operated as the first and second working electrodes. All potentials are reported vs. Ag/AgCl at 300 K. Both the reference electrode and auxiliary electrode were immersed in a 200 μL solution inside a 8 mm diameter PDMS reservoir. In all CV measurements, the potential of the bottom electrodes was swept, and the top electrodes were either held at a constant potential (GC mode) or disconnected (non-GC mode).

Results and discussion

Fabrication of high density metal nanopore templates

A key part of our strategy to study the electrochemical behavior of single molecules involves the preparation of high density arrays of zeptoliter-volume nanopores with internal annular ring and disk electrodes. Previous studies from our laboratory^{17,20} have demonstrated that the size of nanopore-embedded electrodes prepared by NSL is determined by the initial size of the polystyrene sphere and the duration and power of the subsequent O₂ plasma exposure. In order to produce elements with tunable size and spacing, here we utilized nanospheres with initial diameters ranging from 800 nm to 100 nm. Because the initial nanosphere diameter determines the site-to-site spacing in the final structure, starting with smaller diameter nanospheres produces higher density arrays. In addition, smaller initial size nanospheres can be processed using milder plasma treatment conditions to shrink the sphere size, thereby minimizing deformation of the nanospheres which can lead to non-uniform structures.

To test this fabrication scheme, nanospheres with initial diameters ranging from 800 nm, to 200 nm were first assembled on a glass slide and then exposed to an O₂ plasma in order to decrease the size of the nanospheres through isotropic etching.³⁷ Fig. 1 shows the dependence of the final nanosphere size on the duration of O₂ plasma etching. At shorter etching times, the average nanosphere size decreases monotonically with O₂ plasma exposure, and the resulting spheres exhibit smooth, spherical surfaces with the periodic structure of the nanosphere array being well preserved. At longer times (t > 240 s) the final nanosphere size becomes less sensitive to the etching time, and the surface of the resulting spheres is rougher. Based on these observations, the usable processing regime extends from the original diameter, d_0 , to $\sim d_0/3$.

After shrinking the nanosphere size by O2 plasma treatment, a 10 nm Cr layer was deposited uniformly over the etched nanosphere array. Then the nanospheres were removed by sonication in chloroform, revealing a Cr nanopore

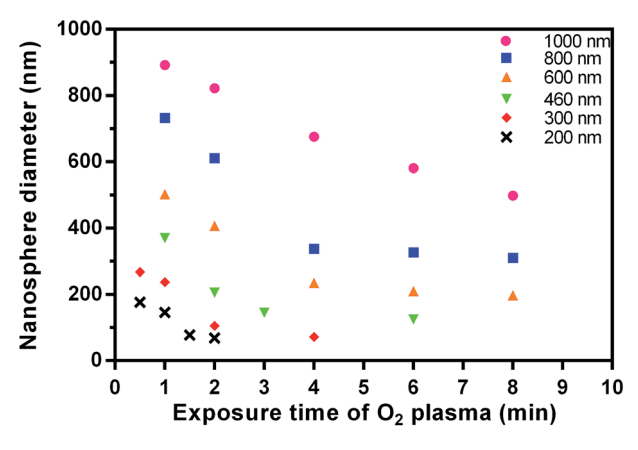


Fig. 1 The dependence of final nanosphere size on O₂ plasma exposure time for polystyrene nanospheres with initial diameters of 1000 nm (pink), 800 nm (blue), 600 nm (orange), 460 nm (green), 300 nm (red), and 200 nm (black).

mask. Cr was chosen as an etch mask based on its good adhesion to SiO₂ (passivating layer for the electrochemical device) and its selectivity in subsequent dry etching steps. Fig. 2 shows scanning electron microscope (SEM) images of nanopore arrays with a variety of pore sizes and spacings. The pore size could be adjusted from 800 nm to 50 nm, and the pore density could be controlled from low ($\sim 10^8$ cm⁻²) to high density ($\sim 10^{10}$ cm⁻²) by varying the O₂ plasma exposure conditions and the initial size of nanospheres, respectively. At the smallest initial nanosphere diameter, $d_0 = 100$ nm, the translational symmetry of the arrays was degraded relative to arrays produced from larger d_0 values. These images clearly demonstrate that NSL is a flexible, high-fidelity method to fabricate well-ordered, high-density nanopore arrays.

Fabrication of high density dual nanopore electrode arrays (NEAs)

Dual NEAs are nanopore arrays in which each nanopore has two electrodes, constructed in a metal-insulator-metal (MIM) structure in the vertical direction, as illustrated schematically in Fig. 3(A). First, the electrode pattern and the intersecting area of the two electrode layers, i.e. bottom disk electrode and top ring electrode, were defined by photolithography. The thicknesses of the metal and insulating layers were controlled by metal deposition and chemical vapor deposition, respectively. Then the metal nanopore template was fabricated on top of the intersecting electrodes. Finally, the dual NEAs were produced by dry etching to propagate the nanopore-templated pattern through to the bottom metal disk, at which the etch was stopped. Well ordered NEAs with tunable pore size and spacing were achieved at large scale, viz. Fig. 3(B). The cross-sectional SEM image, Fig. 3(C), shows the MIM structure in the NEA, each pore exhibiting

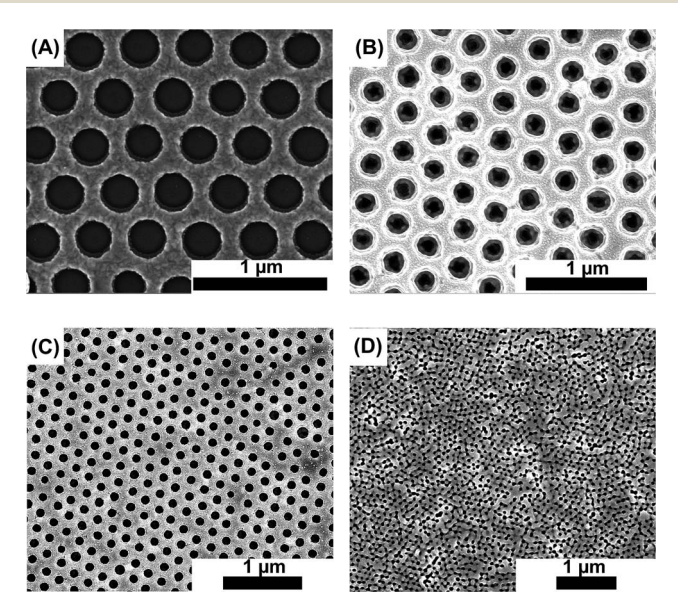


Fig. 2 SEM images of nanopore arrays with different pore diameters and densities. From (A) to (D), the initial sizes of nanosphere templates are 460 nm, 300 nm, 200 nm and 100 nm, respectively.

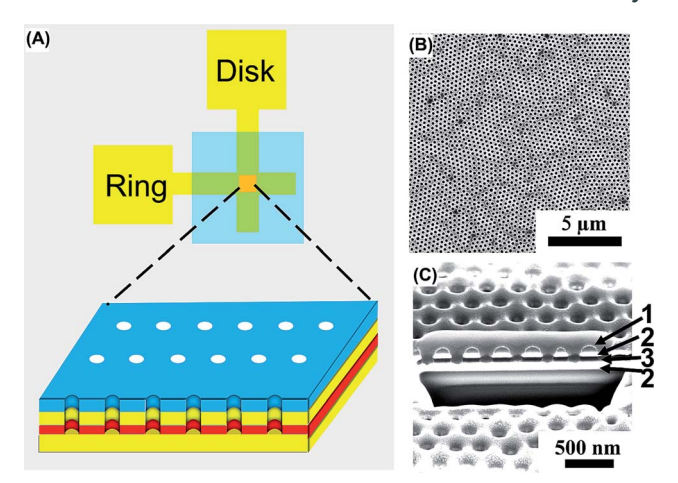


Fig. 3 (A) Schematic diagram showing the layout of a high density nanoscale RRDE array, with each nanopore consisting of an MIM structure in the vertical direction. (B) Plan view and (C) cross-sectional SEM images of the RRDE array. From top to bottom, the grey (1), white (2), black (3), and white (2) layers in (C) indicate SiO2, Au, SiNx, and Au layers, respectively.

from top to bottom: SiO_2 protection layer (grey), top Au ring electrode (white), SiN_x insulating layer (black) and bottom Au disk electrode (white). The average bottom and top diameters for this particular conical structure are ca. 90 nm and 150 nm, respectively.

Considering that the combined thickness of the top Au layer and SiN_x layer is \sim 150 nm, and that the nanopore shape is a right circular conical frustum, the effective volume of the ring-disk electrode region of each nanopore, i.e. the volume pertinent to the redox cycling reaction is $\sim 1.25 \times 10^{-18}$ L. Thus, the concentration corresponding to single molecule occupancy is \sim 1.3 μ M. However, both the pore volume and the pore spacing are important for functional analysis of the electrochemical behavior of NEAs - the pore volume setting the single molecule occupancy criteria, and the pore spacing determining the ability to recapture molecules that escape from a given pore in neighboring pores. The limitations on fabricating NEAs with high pore densities and small pore volumes by the NSL-templating strategy employed here arises due to the uniformity of the etching process when the top diameter of the nanopore is smaller than 100 nm. Additionally, the thickness of the top SiO₂ layer is important to achieve uniform shapes and small diameter nanopore arrays. In order to balance pore density against the requirement to operate with well-structured nanopores for electrochemical measurements, the smallest initial nanosphere size used to fabricate NEAs for electrochemical measurements was 300 nm, corresponding to the image in Fig. 2(B). This design rule produces arrays with pore densities, $ho_{
m p}\sim 10^9~{
m cm}^{-2}$, which combined with an intersecting electrode area of 150 μ m \times 150 μ m, leads to arrays with \sim 225 000 pores.

Current amplification in NEAs

The unique geometry of the dual NEA, i.e. two individually addressable and closely spaced working electrodes within an ultrasmall volume nanopore, is

a nearly ideal geometry for investigating the redox cycling reaction of small numbers of reversible electroactive species. Here, the bottom (disk) and top (ring) electrodes were used as generator and collector electrodes, respectively, during redox cycling experiments. Accordingly, species that are oxidized (reduced) at the bottom electrode can be reduced (oxidized) when efficiently captured by the top electrode. Furthermore, given the ~100 nm spacing between generator and collector, diffusion times between the electrodes for typical redox species in aqueous electrolyte are of the order of a few us.

Fig. 4(A) shows typical cyclic voltammograms (CVs) of Ru(NH₃)₆^{2/3+} in 0.1 M KCl obtained by scanning the bottom electrode while floating (non-GC mode, black line) or holding the top electrode at +0.1 V (GC mode, red line) or -0.4 V (GC mode, blue line) vs. Ag/AgCl on an array with 400 nm pore size and 460 nm pore-to-pore spacing. When operated in non-GC mode at a scan rate of 100 mV s⁻¹, the nanoscale RRDE array behaves like a single recessed microelectrode of the same electrode size (150 μ m imes 150 μ m). Under non-GC mode conditions, a characteristic transport-limited CV (inset of Fig. 4(A)) with substantial capacitive contribution was observed. This is likely due to the overlap of diffusion zones of neighboring nanopore electrodes.40 Using a model developed by Bond et al.,41 a current of ~57 nA was calculated for a single recessed microelectrode of the same electrode size and depth as the nanoscale RRDE array. This value agrees well with the 56 nA peak current observed experimentally. When the potential of the top electrode was fixed to either a relatively reducing (-0.4 V) or oxidizing (0.1 V)value for Ru(NH₃)₆^{2/3+}, the limiting current of the RRDE array in GC-mode was significantly enhanced. The amplification of measurable current from 60 nA (solid, black line) to 3.30 μA (solid, red line) is clear evidence that the analyte undergoes redox cycling. The amplification factor for redox cycling (AF_{RC}), calculated from the ratio of limiting current in GC mode to that in non-GC mode, is $AF_{RC} = 55$ under these conditions.

AF_{RC} is strongly related to the collection efficiency of the generator-collector system, which is defined as the ratio of the limiting current at the collector electrode to that at the generator electrode. In the structures studied here, collection efficiencies for the top electrode, Φ_t , as high as 99.4% ($d_0 = 400$ nm, 460 nm spacing, $E_{\text{top}} = +0.1 \text{ V}$) were measured. If the fixed potential of the top electrode is switched from +0.1 V to -0.4 V vs. Ag/AgCl, the analyte oxidized at the bottom electrode is then reduced at the top electrode. Under these conditions, the limiting currents for top and bottom electrodes were 3.51 µA (dashed blue line) and 3.47 µA (solid blue line), respectively, which gives the collection efficiency of the bottom electrode as $\Phi_{\rm b}=98.9\%$. Based on the theory of Tabei and coworkers,25 the number of redox cycles NRC can be estimated from,

$$N_{\rm RC} = \frac{1}{1 - \Phi_{\rm t} \Phi_{\rm b}} \tag{1}$$

For the nanoscale RRDE array described above, Φ_t and Φ_b were 99.4% and 98.9%, respectively, yielding $N_{\rm RC}=57.7$, in excellent agreement with the experimentally measured value of AFRC. This value is substantially higher than previously reported AF_{RC} values obtained from lower density RRDE arrays, 19 an observation that can be attributed to the higher array density and smaller pore size, both of which work to improve the redox cycling efficiency.

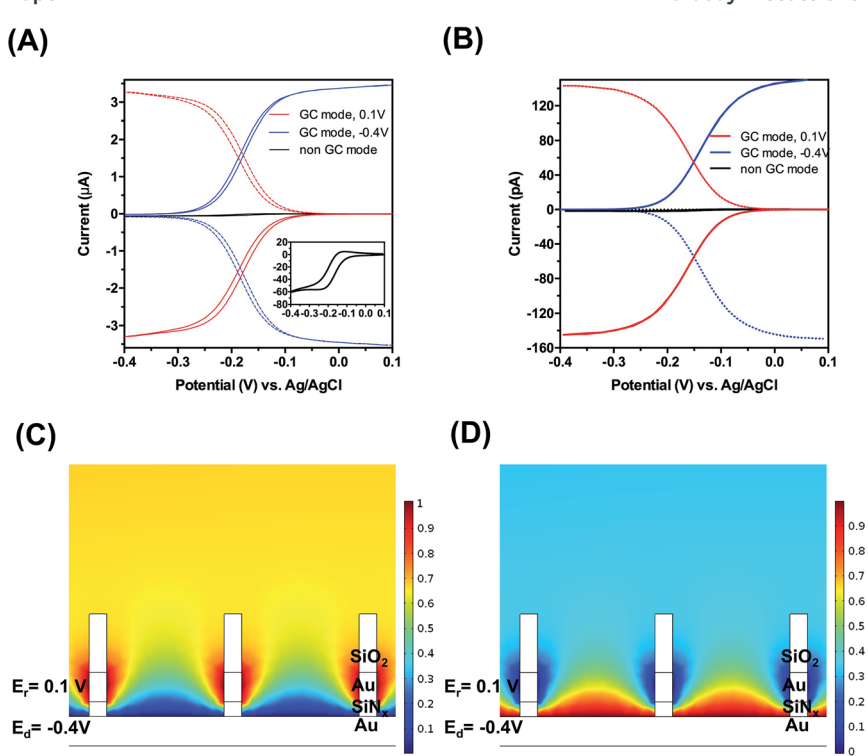


Fig. 4 (A) Cyclic voltammograms of 1 mM Ru(NH₃) $_6^{3+}$ on the nanoscale RRDE array ($d_0 =$ 400 nm, 460 nm spacing) obtained by sweeping the bottom disk electrode while at the same time holding the top ring electrode at +0.1 V (red), -0.4 V (blue) or floating (black) in 0.1 M KCl. (Inset) magnified version of the CV obtained with the ring electrode floating. Current in nA. (B) Simulated CV response of an array of 10 nanopore electrodes under the same measurement conditions. In (A) and (B) dashed lines give current at the collector electrode while the generator electrode is swept. (C) and (D) Spatial distribution of $Ru(NH_3)_6^{3+}$ inside and outside the pore region taken from simulations of an array of 10 nanopore electrodes under conditions where the top ring electrode is held at an oxidizing (C) or reducing (D) potential. Scale bars in (C) and (D) are normalized to the maximum concentration.

Fig. 4(B) shows simulated CVs of nanoscale RRDE arrays with the same geometric parameters as the experimental structure, with the top electrode held at +0.1 V (red line), -0.4 V (blue line) or floating (black line). The simulated singlenanopore limiting current (\sim 15 pA) is somewhat smaller than the experimental value (~30 pA) obtained through dividing the total limiting current (3.30 μA) by the number of nanopores (\sim 112 500) on the array. The simulated amplification factor $AF_{sim} = 54.8$ calculated from the ratio of the simulated limiting currents in GC mode to that in non-GC mode agrees very well with the experimental AF_{RC} = 55. The calculated spatial distributions of redox species under different applied potentials are shown in Fig. 4(C) and (D), with the top ring electrode potential held at +0.1 V and -0.4 V vs. Ag/AgCl, respectively. With the top electrode set at an oxidizing potential, Fig. 4(C), Ru(NH₃)₆²⁺ reduced at the bottom disk electrode is efficiently oxidized to Ru(NH₃)₆³⁺ at the top ring electrode. Interestingly, the simulated spatial distributions reveal pockets of unreacted Ru(NH₃)₆³⁺ near the surface of the insulator in Fig. 4(C). Conversely, when the top electrode is set to a negative potential (-0.4 V), Fig. 4(D), $\text{Ru}(\text{NH}_3)_6^{3+}$ produced at the bottom electrode is reduced at the top electrode.

Effect of pore size and spacing

The characteristic collision times of molecules with the electrodes inside the nanopores depend strongly on pore size. On the other hand, the recapture of escaped molecules by adjacent nanopore-embedded electrodes depends largely on pore density. Thus, the collection efficiency and the current amplification should depend strongly on the geometry of the array. Both experiments and simulations were conducted to understand the dependence of RC response on the nanopore geometry, especially the effect of pore size and pore density, on the efficiency of redox cycling.

Table 1 shows the experimental and simulated AF values for nanoscale RRDE arrays with different pore spacings, $S_{\rm p}$. A series of nanoscale RRDE arrays were fabricated by using nanospheres with different initial diameters (800 nm, 600 nm, 460 nm), each template being reduced to the same sphere size (\sim 200 nm) by O_2 plasma etching to produce a series of structures with constant pore size but varying pore density. The electrochemical behavior of these structures was then compared to finite element simulations performed to probe the effect of pore spacing on AF. As shown in Table 1, both simulated and experimental AF values increase with decreasing pore spacing. This is likely due to overlapping diffusion zones on high density nanoscale RRDE arrays, as is evident in the simulated concentration distributions in Fig. 4(C) and (D). At high pore densities the overlapping diffusion zones improve the collection efficiency by recapturing any molecules that escape from a neighboring nanopore.

The dependence of AF on pore size was also investigated on a series of nanoscale RRDE arrays of constant pore spacing but different pore diameters. These structures were prepared by starting from NSL templates with the same initial nanosphere diameter, but then exposing them to O_2 plasma for differing times to produce different final pore diameters. The simulated and experimental AF values of this series are summarized in Table 2. Both show that AF increases with increasing nanopore diameter, reflecting a larger net capture efficiency for larger pores, thus giving rise to larger AF $_{\rm RC}$. At these small sizes, this likely reflects the effect of $\Phi_{\rm b}$, which increases at larger disk electrode sizes. This was confirmed by simulations which illustrate that $\Phi_{\rm b}$ increases with increasing nanopore diameter (Table 2).

Linear response and scan rate dependence

In order to test the performance of the high density nanopore electrode arrays to small molecular loadings, the whole array was operated in GC mode to detect

Table 1	Experimental and simulated AF values as a function of pore spacing (S_p)						
S_{p}	460	600	800	1000			
AF_{exp}	38.1	35.0	32.1	20^a			
AF_{sim}	47.2	36.2	28.8	21.1			

^a Value is adopted from ref. 19.

Table 2 Experimental and simulated AF values and collection efficiencies as a function of pore diameter (D_n)

D_{p}	400	350	300	250	200
AF_{exp}	54.8	40.8	31.0	23.6	21.8
AF_{sim}	55.4	54.1	52.1	49.5	46.1
$arPhi_{ m t}$	99.1%	99.3%	99.4%	99.6%	99.7%
$\Phi_{ m b}$	98.7%	98.5%	98.3%	98.1%	97.7%

redox species of Ru(NH₃)₆³⁺ at concentrations down to 100 nM. The limiting voltammetric current obtained from Ru(NH₃)₆³⁺ as a function of concentration in GC mode is displayed in Fig. 5(A), illustrating that it is linear over 5 orders of magnitude in concentration. The current signals in these experiments were collected from a 150 µm × 150 µm nanopore electrode array with a (top) pore diameter and spacing of 150 nm and 300 nm, respectively. In this geometry, the conical frustum gives an average pore diameter ~ 150 nm at the top and ~ 90 nm at the bottom. Considering that the combined thickness of the top Au and SiN_r layers is 150 nm, the effective volume for redox cycling reaction is 1.25 aL. In order to obtain single molecule occupancy, the required concentration of analyte is \sim 1.3 µM. As shown in Fig. 5(A), the limiting current at 1 µM was \sim 0.4 nA, which means on average each nanopore produced ~1.8 fA current signal under these conditions (\sim 225 000 pores on the entire array) corresponding to ca. 10⁴ electron transfer events per second, a realistic value given an estimated diffusion time of 10 μ s. This value is \sim 10 \times smaller than the value (20 fA) reported by Lemay and coworkers from single molecule diffusion inside an opposed-planar electrode nanofluidic electrochemical device.³² We attribute this to the lower collection efficiency of the open geometry of nanopore electrodes compared to the closed structure used by Lemay's group.

Another advantage of high density nanopore electrode arrays is the small capacitive current in GC mode, as shown in Fig. 5(B). At high electrolyte concentrations, such as those used here, the magnitude of the charging current for nanoelectrodes is typically comparable to the faradaic current at low analyte concentrations. Here, the measured charging current at both the top and bottom

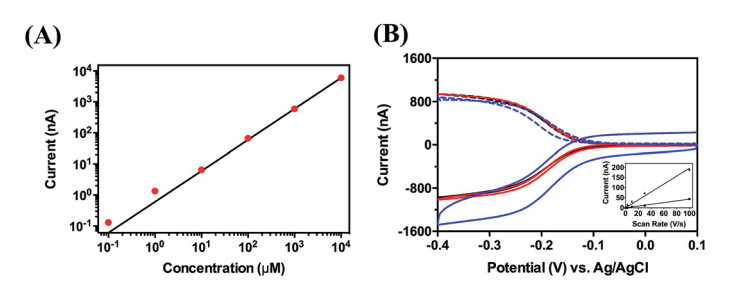


Fig. 5 (A) Limiting GC-mode currents for different concentrations of Ru(NH₃)₆³⁺ with aqueous 0.1 M KCl on the nanoscale RRDE array ($d_0 = 150$ nm, 300 nm spacing). (B) Cyclic voltammograms of 1 mM $Ru(NH_3)_6^{3+}$ solution with 0.1 M KCl as a function of scan rate. Bottom disk electrode is swept at 100 V s^{-1} (blue), 3 V s^{-1} (red) and 0.1 V s^{-1} (black); current acquired at ring (dashed) and disk (solid) electrodes. (Inset) capacitive current of ring (lower line) and disk (upper line) electrode as a function of scan rate.

electrode increases linearly with the scan rate ranging from $0.1 \, \mathrm{V \, s^{-1}}$ to $100 \, \mathrm{V \, s^{-1}}$, viz. Fig. 5(B) inset. However, the capacitance of the whole array had little effect on the voltammetric signal when the scan rate was below 1 V s⁻¹. The smaller capacitive current ($\sim 0.2 \, \mathrm{nA}$) of the top electrode even at scan rates as high as $100 \, \mathrm{V \, s^{-1}}$ indicates that these devices may serve as a suitable electrode platforms for ultrafast electrochemistry, as well as single molecule, measurements.

Conclusion

In this work we demonstrate a simple and robust approach to fabricate high density nanopore arrays with well-controlled dual-electrodes for ultrahigh efficiency redox cycling. Nanosphere lithography and O_2 plasma etching are clearly competent to fabricate nanopore arrays with controlled pore diameter and spacing over a wide range. Electrochemical reactions of redox couples operated in generator and collector mode produced greatly enhanced currents relative to non-GC operation, with collector electrode collection efficiencies as high as $\Phi_t = 99.4\%$. Both experiments and simulations illustrate the significance of pore size and spacing in determining high performance redox cycling.

The nanoscale RRDE arrays developed and studied here represent a new part of electrochemical phase space, where the small electrochemical detection volume (\sim 1 aL) of each nanopore means that single molecule occupancy can be achieved at μ M concentrations. In fact, at the lowest concentration at which a chemically significant electrochemical signal was measured (100 nM), the average occupancy was $\langle n \rangle \sim 0.13$. This measurement was enabled by a combination of high redox cycling collection efficiency at both bottom and top electrodes, $\Phi_{\rm b,t} \sim 99\%$, and a massively parallel array of 2.25×10^5 pores giving rise to aggregate signals significantly above the noise level. Furthermore, these large area nanoscale RRDE arrays exhibit insignificant charging current at scan rates below 1 V s⁻¹ and acceptable charging currents at scan rates as high as 100 V s⁻¹, suggesting their use for simultaneous ultrafast, ultrasensitive electrochemical measurements.

Acknowledgements

This work was supported by the National Science Foundation grant 1404744 (K. F. and C. M.) and the Defense Advanced Research Projects Agency FA8650-15-C-7546 (D. H.). Fabrication and structural characterization of the devices studied here were accomplished at the Notre Dame Nanofabrication Facility and the Notre Dame Integrated Imaging Facility, whose generous support is gratefully acknowledged.

References

- 1 D. W. M. Arrigan, Analyst, 2004, 129(12), 1157-1165.
- 2 J. T. Cox and B. Zhang, Annu. Rev. Anal. Chem., 2012, 5(1), 253-272.
- 3 S. M. Oja, M. Wood and B. Zhang, Anal. Chem., 2013, 85(2), 473-486.
- 4 S. M. Oja, Y. Fan, C. M. Armstrong, P. Defnet and B. Zhang, *Anal. Chem.*, 2016, 88(1), 414–430.
- 5 K. Dawson and A. O'Riordan, Annu. Rev. Anal. Chem., 2014, 7(1), 163-181.

- 6 R. W. Murray, Chem. Rev., 2008, 108(7), 2688-2720.
- 7 D. Krapf, M.-Y. Wu, R. M. M. Smeets, H. W. Zandbergen, C. Dekker and S. G. Lemay, Nano Lett., 2006, 6(1), 105-109.
- 8 G. Wang, B. Zhang, J. R. Wayment, J. M. Harris and H. S. White, J. Am. Chem. Soc., 2006, 128(23), 7679-7686.
- 9 A. P. Ivanov, K. J. Freedman, M. J. Kim, T. Albrecht and J. B. Edel, ACS Nano, 2014, 8(2), 1940-1948.
- 10 W. Cheng, S. Dong and E. Wang, Anal. Chem., 2002, 74(15), 3599-3604.
- 11 V. P. Menon and C. R. Martin, Anal. Chem., 1995, 67(13), 1920–1928.
- 12 Y. H. Lanyon, G. De Marzi, Y. E. Watson, A. J. Quinn, J. P. Gleeson, G. Redmond and D. W. M. Arrigan, Anal. Chem., 2007, 79(8), 3048-3055.
- 13 M. E. Sandison and J. M. Cooper, Lab Chip, 2006, 6(8), 1020-1025.
- 14 F. Santoro, S. Dasgupta, J. Schnitker, T. Auth, E. Neumann, G. Panaitov, G. Gompper and A. Offenhäusser, ACS Nano, 2014, 8(7), 6713-6723.
- 15 C. N. LaFratta and D. R. Walt, Chem. Rev., 2008, 108(2), 614-637.
- 16 C. Ma, N. M. Contento, L. R. Gibson and P. W. Bohn, Anal. Chem., 2013, 85(20), 9882-9888.
- 17 C. Ma, W. Xu, W. R. A. Wichert and P. W. Bohn, ACS Nano, 2016, 10, 3658-3664.
- 18 C. Ma, L. P. Zaino III and P. W. Bohn, Chem. Sci., 2015, 6(5), 3173-3179.
- 19 C. Ma, N. M. Contento and P. W. Bohn, J. Am. Chem. Soc., 2014, 136(20), 7225-7228.
- 20 C. Ma, N. M. Contento, L. R. Gibson and P. W. Bohn, ACS Nano, 2013, 7(6), 5483-5490.
- 21 D. H. Han, L. P. Zaino III, K. Fu and P. W. Bohn, J. Phys. Chem. C, 2016, DOI: 10.1021/acs.jpcc.6b01287.
- 22 E. O. Barnes, G. E. M. Lewis, S. E. C. Dale, F. Marken and R. G. Compton, Analyst, 2012, 137(5), 1068-1081.
- 23 A. Frumkin, L. Nekrasov, B. Levich and J. Ivanov, J. Electroanal. Chem., 1959, 1(1), 84-90.
- 24 S. Bruckenstein and B. Miller, Acc. Chem. Res., 1977, 10(2), 54-61.
- 25 O. Niwa, M. Morita and H. Tabei, Anal. Chem., 1990, 62(5), 447-452.
- 26 A. J. Bard, J. A. Crayston, G. P. Kittlesen, T. Varco Shea and M. S. Wrighton, Anal. Chem., 1986, 58(11), 2321-2331.
- 27 E. Goluch, B. Wolfrum, P. Singh, M. G. Zevenbergen and S. Lemay, Anal. Bioanal. Chem., 2009, 394(2), 447-456.
- 28 F.-R. F. Fan and A. J. Bard, Science, 1995, 267(5199), 871–874.
- 29 A. J. Bard and F.-R. F. Fan, Acc. Chem. Res., 1996, 29(12), 572-578.
- 30 F.-R. F. Fan, J. Kwak and A. J. Bard, J. Am. Chem. Soc., 1996, 118(40), 9669-9675.
- 31 M. A. G. Zevenbergen, D. Krapf, M. R. Zuiddam and S. G. Lemay, Nano Lett., 2006, 7(2), 384-388.
- 32 M. A. G. Zevenbergen, P. S. Singh, E. D. Goluch, B. L. Wolfrum and S. G. Lemay, Nano Lett., 2011, 11(7), 2881-2886.
- 33 T. Li, L. Su, W. Hu, H. Dong, Y. Li and L. Mao, Anal. Chem., 2010, 82(4), 1521-
- 34 M. Huske, R. Stockmann, A. Offenhausser and B. Wolfrum, Nanoscale, 2014, **6**(1), 589–598.
- 35 U. C. Fischer and H. P. Zingsheim, J. Vac. Sci. Technol., 1981, 19(4), 881-885.

- 36 A. Plettl, F. Enderle, M. Saitner, A. Manzke, C. Pfahler, S. Wiedemann and P. Ziemann, Adv. Funct. Mater., 2009, 19(20), 3279-3284.
- 37 L. Ji, Y.-F. Chang, B. Fowler, Y.-C. Chen, T.-M. Tsai, K.-C. Chang, M.-C. Chen, T.-C. Chang, S. M. Sze, E. T. Yu and J. C. Lee, Nano Lett., 2014, 14(2), 813-818.
- 38 G. D. Moon, T. I. Lee, B. Kim, G. Chae, J. Kim, S. Kim, J.-M. Myoung and U. Jeong, ACS Nano, 2011, 5(11), 8600-8612.
- 39 A. V. Whitney, B. D. Myers and R. P. Van Duyne, Nano Lett., 2004, 4(8), 1507-1511.
- 40 A. Wahl, K. Dawson, J. MacHale, S. Barry, A. J. Quinn and A. O'Riordan, Faraday Discuss., 2013, 164(0), 377-390.
- 41 A. M. Bond, D. Luscombe, K. B. Oldham and C. G. Zoski, J. Electroanal. Chem. Interfacial Electrochem., 1988, 249(1), 1-14.